RESEARCH ARTICLE

Characteristics of the potential vorticity and its budget in the surface layer over the Tibetan plateau

Chen Sheng[1,2] | Guoxiong Wu[1,2*] | Yiqiong Tang[1,3] | Bian He[1,2,4*] | Yongkun Xie[1] | Tingting Ma[1] | Ting Ma[1,3] | Jinxiao Li[1] | Qing Bao[1,2] | Yimin Liu[1,2,4*]

[1]State Key Laboratory of Numerical Modeling for Atmospheric Sciences and Geophysical Fluid Dynamics (LASG), Institute of Atmospheric Physics, Chinese Academy of Sciences, Beijing, China

[2]College of Earth and Planetary Sciences, University of Chinese Academy of Sciences, Beijing, China

[3]School of Atmospheric Sciences, Nanjing University of Information Science and Technology, Nanjing, China

[4]CAS Center for Excellence in Tibetan Plateau Earth Sciences, Chinese Academy of Sciences (CAS), Beijing, China

Correspondence
Guoxiong Wu, Bian He, and Yimin Liu, LASG, Institute of Atmospheric Physics, Chinese Academy of Sciences, Beijing 100029, China.
Email: gxwu@lasg.iap.ac.cn (G. W.), heb@lasg.iap.ac.cn (B. H.), and lym@lasg.iap.ac.cn (Y. L.)

Abstract

The variability of interior atmospheric potential vorticity (PV) is linked with PV generation at the Earth's surface. The present paper reveals the features of the surface PV and provides a stepping stone to investigate the surface PV budget. In this study, the formats of the PV and PV budget adopting a generalized vertical coordinate were theoretically examined to facilitate the calculation of the surface PV and its budget. Results show that the formats of the PV and PV budget equations are independent of the vertical coordinate. While the vertical component of the surface PV dominates over the platform of the Tibetan Plateau, the horizontal component plays an important role over the slopes of the Tibetan Plateau, especially the southern slope owing to the strong in-situ meridional gradient of the potential temperature. These results indicate that the employment of complete surface PV not only provides a finer PV structure but also more appropriately reveals its effect on atmospheric circulation. Diagnosis based on reanalysis and model output demonstrates that the surface PV budget equation is well balanced both in terms of the climate mean and synoptic process, and the surface PV budget in June has a prominent diurnal cycle. The diabatic heating with a minimum in the early morning and a maximum from evening to midnight contributes dominantly to this diurnal cycle. It is further indicated that positive PV generation due to diabatic heating is essential for the formation, development, and movement of the Tibetan Plateau vortex.

KEYWORDS
diabatic heating, potential vorticity (PV), surface PV, surface PV budget, Tibetan Plateau

1 | INTRODUCTION

Potential vorticity (PV; Rossby, 1940; Ertel, 1942) is a physical quantity that inherently couples atmospheric dynamics and thermodynamics. The examination of PV has clarified a wide range of dynamical phenomena in the field of planetary fluids, primarily owing to the conservation and invertibility properties of PV (e.g., Hoskins *et al.*, 1985). Many aspects of the role of PV in atmospheric general circulation, such as the connection between the isentropic PV anomaly and circulation anomaly (Hoskins *et al.*, 1985; Hoskins, 1997, 2015), the relationship between PV and rainstorms (Wu *et al.*, 1995), and the effects of advective PV flux on the upper tropospheric flow (Liu *et al.*, 2007; Ortega *et al.*, 2018), have been documented. In these studies (e.g., Hoskins *et al.*, 1985; Wu *et al.*, 1995; Hoskins, 1997, 2015; Zhao and Ding, 2009; Luo *et al.*, 2018a, 2018b; Ortega *et al.*, 2018), the redistribution of atmospheric interior PV and its weather and climate effects have been of primary interest.

Meanwhile, the studies of Haynes and McIntyre (1987, 1990) and Hoskins (1991) evoked interest in PV at the Earth's surface. The impermeability theorem of PV proposed by Haynes and McIntyre (1987, 1990) suggests that PV can be neither created nor destroyed for a completely closed isentropic surface. A subdivision of the atmosphere into the Overworld, Middleworld, and Underworld (Figure 1) proposed by Hoskins (1991) showed that there are entirely closed isentropic surfaces in the Overworld and Middleworld, while the isentropic surfaces of the Underworld intersect with the Earth's surface. In terms of the impermeability theorem, Hoskins (1991) demonstrated that total PV is constant in the Overworld and Middleworld but changeable in the Underworld. These studies indicated that the source of global atmospheric PV lies within the Earth's surface. In other words, the globally integrated PV in the atmosphere is determined by its generation at the Earth's surface. Further theoretical studies demonstrated that the variation of PV in the atmospheric interior is closely related to the surface PV, and the PV generated at the surface can be transferred into the atmospheric interior and affects the variation of PV and the associated circulation at a global scale (Held and Schneider, 1999; Schneider, 2005; Egger *et al.*, 2015). However, the potential temperature fluctuates at the Earth's surface and near-surface isentropes may lie above or below the surface, and the investigation of the Earth's surface PV and its budget has thus been difficult.

In addition to the flat surface of the Earth, elevated mountains penetrate isentropic surfaces in the lower troposphere and generate extra internal boundaries of these surfaces as shown in Figure 1, thereby producing additional PV sources for the atmosphere. Aebischer and Schär (1996), Schar *et al.* (2003), and Flamant *et al.* (2004) studied PV around the Alps through observation and numerical simulation and found that the Alps are a source of PV anomalies in the lower troposphere and generate a wake structure with numerous elongated filaments of anomalous PV (i.e., PV banners) that affects downstream windstorms. The gigantic Tibetan Plateau (TP), as the highest and broadest plateau in the world, intensively intersects with many isentropic surfaces in
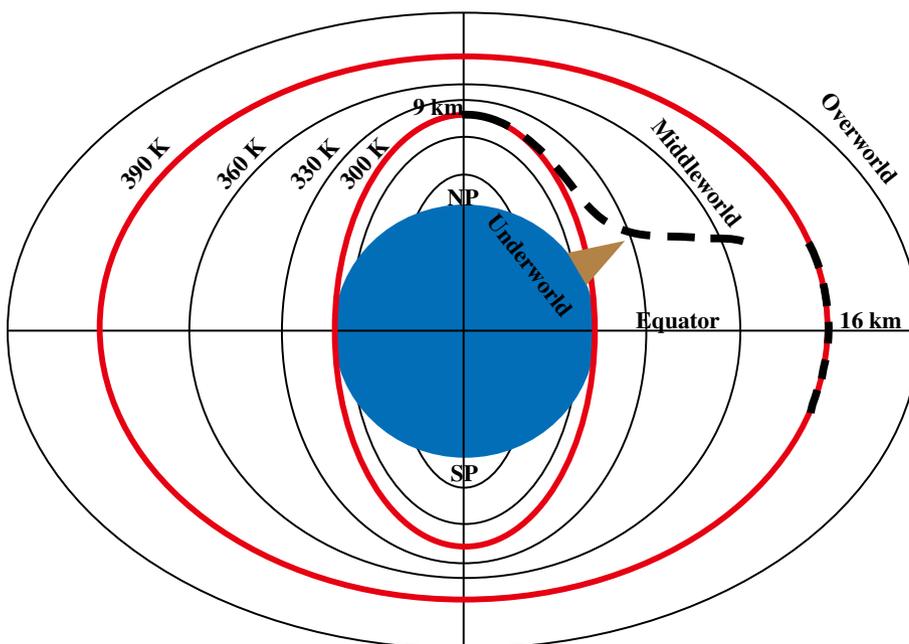

FIGURE 1 Schematic distributions of isentropic surfaces and the threefold world. Solid and dashed black lines respectively indicate isentropic surfaces and the atmospheric tropopause. The blue circle represents the Earth while the brown triangle represents the TP. The North and South Poles are respectively denoted NP and SP

the lower troposphere (Wu *et al.*, 2007, 2018). According to the impermeability theorem, the TP generates a great deal of PV that can be transported into the atmospheric interior (Hoskins, 1991; Ren *et al.*, 2014; Yu *et al.*, 2019; Ma *et al.*, 2019). Given the huge global weather and climate effects of the TP (e.g., Flohn, 1957; Ye *et al.*, 1957; Ye and Gao, 1979; Yanai *et al.*, 1992; Wu *et al.*, 2012; Xu *et al.*, 2015; Ren *et al.*, 2019), the associated surface PV and surface PV generation of the TP need to be further explored.

One of the great challenges in studying the surface PV over the TP is that the traditional PV and PV budget are calculated in a pressure or an isentropic coordinate system. As documented above, because the higher pressure level or lower isentropic level is under the mountain surface, there is no data across the wide terrain. Thus, it is almost impossible to calculate the surface PV and surface PV budget directly in the pressure or isentropic coordinate system. The method of interpolating the pressure coordinate system to the terrain-following η coordinate system is widely adopted, but introduces a high interpolation error (Li *et al.*, 2017). Cao and Xu (2011) derived the PV formula in the terrain-following η coordinate system, but many reanalysis model datasets are archived in the hybrid σ–p coordinate system. Although the second Modern-Era Retrospective Analysis for Research and Applications (MERRA2) reanalysis dataset provides PV in the hybrid σ–p coordinate system, the PV product neglects the horizontal component of PV, which could be important in regions with topographic relief. It remains difficult to accurately calculate the PV and PV budget at the Earth's surface, particularly in mountainous areas.

The present paper aims at improving the understanding of the surface PV and providing a stepping stone to investigate the surface PV budget. To this end, we developed an algorithm that calculates the surface PV and surface PV budget and examined the characteristics of surface PV and its budget in the TP area. The remainder of the paper is organized as follows. Section 2 presents the data and model used in the study. Section 3 introduces algorithms for the calculation of surface PV and its budget. Section 4 analyses the spatial and temporal distributions of the surface PV. Additionally, the vertical and horizontal components of PV in the TP area in reanalysis and model output are compared. Characteristics of the surface PV budget, particularly the diurnal cycle, are investigated in Section 5. The effects of such a diurnal cycle on the formation and development of a Tibetan Plateau vortex (TPV) are briefly presented. Finally, a summary and discussion are provided in Section 6.

2 | DATA AND MODEL

2.1 | Data

We used monthly mean data on the hybrid σ–p model level obtained from MERRA2 for the period 1980–2014 (Rienecker *et al.*, 2011; Lucchesi, 2012). We employed the air temperature, zonal and meridional wind speeds, and pressure in calculating the surface PV for each month. Climate mean values calculated over June, July, and August (JJA) and over December, January, and February (DJF) were respectively used to represent the boreal summer and winter conditions. The horizontal resolution of all MERRA2 data was $0.625° \times 0.5°$ (longitude $\times$ latitude).

Three-hourly data of the MERRA2 hybrid σ–p model level, including the air temperature, zonal and meridional wind speeds, vertical velocity, and pressure, for the period 2010–2017 were adopted to analyse the climate mean surface PV budget in June. Data for 27 to June 29, 2016 (universal time) were also used to analyse the surface PV budget during a TPV process.

2.2 | Model

The model adopted in this study was the Flexible Global Ocean–Atmosphere–Land System (FGOALS-f2) climate model of the Chinese Academy of Sciences, which was developed at the Institute of Atmospheric Physics/State Key Laboratory of Numerical Modeling for Atmospheric Sciences and Geophysical Fluid Dynamics (Bao *et al.*, 2018). The atmospheric component of FGOALS-f2 is FAMIL2. The FAMIL2 adopts a three-dimensional finite-volume dynamical core (Lin, 2004) over cubed-sphere grids (Putman and Lin, 2007) with six tiles over the globe, which approximates a horizontal resolution of $1° \times 1°$. The hybrid σ–p coordinates have 32 layers, with the model top being at 2.16 hPa. A detailed physical configuration of the model was presented by He *et al.* (2019, 2020).

Two AGCM experiments based on FAMIL2 were conducted. The first experiment was an AMIP standard experiment conducted to characterize the climate mean surface PV. Monthly mean data of the FAMIL2 hybrid σ–p model level were generated for the period 1979–2014. The period 1980–2014 was selected to ensure consistency with the time range of the MERRA2 data.

In the second experiment, the generation and early evolution of a TPV from June 27 to June 29, 2016, were simulated. The forcing sea surface temperature data used to drive FAMIL2 were taken from Optimum Interpolation Sea Surface Temperature version 2 (OISSTv2) (Reynolds

et al., 2007; Banzon et al., 2016; Li et al., 2019). Because each term in the PV equation involves a product of two different variables, and because the reanalysis adopted in this study only provides data at three-hourly resolution, the contribution of the transient processes to the total budget may not be presented properly. To address this problem, we produced a dataset with high time resolution of a half hour for the same period by nudging the FAMIL2 to the MERRA2 reanalysis. A nudging method, which involves the addition of terms to the atmospheric equations to relax the predicted state variables toward the reanalysis at 30-min intervals, was adopted to generate a fine-resolution dataset (Hoke and Anthes, 1976). On the grounds of stability, nudging was performed for January 1 to June 30, 2016. The atmospheric variables used for nudging were the surface pressure, surface geopotential height, three-dimensional atmospheric wind field, and temperature field. The integration time step was set at 30 min. Variables, namely the surface wind, temperature, and pressure, were then used to calculate the surface PV and its budget according to the method introduced in Section 3.

3 | PV, PV BUDGET EQUATION, AND VERTICAL-COORDINATE INDEPENDENCE

3.1 | PV and PV budget equation

According to Ertel (1942), the vector form of PV (P) in the z coordinate system and its budget equation are

$$P = \alpha_z \vec{\xi}_{az} \cdot \nabla_z \theta, \tag{1}$$

$$\frac{dP}{dt} = \alpha_z \xi \rightarrow_{az} \cdot \nabla_z \dot{\theta} + \alpha_z \nabla_z \times \vec{F}_f \cdot \nabla_z \theta, \tag{2}$$

where $\nabla_z \equiv \left(\frac{\partial}{\partial x}, \frac{\partial}{\partial y}, \frac{\partial}{\partial z}\right)$, $\alpha_z = \frac{1}{\rho}$ is the specific volume, ρ is the density, $\vec{\xi}_{az} = \nabla_z \times \vec{V} + f\vec{k}$ is the three-dimensional absolute vorticity vector, $\vec{V} = (u,v,w)$ is the three-dimensional wind vector, θ is the potential temperature, $\dot{\theta} = \frac{d\theta}{dt}$ is the diabatic heating rate, $\vec{F_f} = (F_x, F_y)$ is the frictional force, and the subscript z indicates the z coordinate system.

3.2 | Vertical-coordinate independence of PV and the PV budget equation

For large-scale motion, $\left|\frac{\partial w}{\partial x}\right|$ and $\left|\frac{\partial w}{\partial y}\right|$ have an order of magnitude of 10^{-8} while $\left|\frac{\partial u}{\partial z}\right|$ and $\left|\frac{\partial v}{\partial z}\right|$ have an order of

magnitude of 10^{-3}. The horizontal change of the vertical velocity in the horizontal vorticity can therefore be ignored with high accuracy in the z coordinate system, and the scalar form of PV in the z coordinate system is

$$P = \alpha_z \left\{ -\frac{\partial v}{\partial z}\left(\frac{\partial \theta}{\partial x}\right)_z + \frac{\partial u}{\partial z}\left(\frac{\partial \theta}{\partial y}\right)_z + \left[f + \left(\frac{\partial v}{\partial x}\right)_z - \left(\frac{\partial u}{\partial y}\right)_z \right]\frac{\partial \theta}{\partial z} \right\}. \tag{3}$$

Introducing a generalized vertical coordinate system (x, y, e, t) for any variable F, $F(x, y, e, t) = F(x, y, z (x, y, e, t), t)$, where e is a monotonic function of z in the vertical direction and the vertical axis of the e coordinate system (with e usually being equal to p, z or θ). According to the chain rule, we have

$$\left.\begin{aligned} \left(\frac{\partial F}{\partial x}\right)_e &= \left(\frac{\partial F}{\partial x}\right)_z + \frac{\partial F}{\partial z}\left(\frac{\partial z}{\partial x}\right)_e \\ \left(\frac{\partial F}{\partial y}\right)_e &= \left(\frac{\partial F}{\partial y}\right)_z + \frac{\partial F}{\partial z}\left(\frac{\partial z}{\partial y}\right)_e \\ \frac{\partial F}{\partial e} &= \frac{\partial F}{\partial z}\frac{\partial z}{\partial e} \end{aligned}\right\}. \tag{4}$$

Letting α_e indicate the specific volume in the e coordinate system, we have $\delta m = \frac{1}{\alpha_z}\delta x \delta y \delta z = \frac{1}{\alpha_e}\delta x \delta y \delta e$; thus,

$$\alpha_e = \alpha_z \frac{\partial e}{\partial z}. \tag{5}$$

The PV in the e coordinate system (P_e) is defined to have the same form as that in the z coordinate system; that is, the symbols imitate those in formula (3) and we have

$$\begin{aligned} P_e &= \alpha_e \vec{\xi}_{ae} \cdot \nabla_e \theta \\ &= \alpha_e \left\{ -\frac{\partial v}{\partial e}\left(\frac{\partial \theta}{\partial x}\right)_e + \frac{\partial u}{\partial e}\left(\frac{\partial \theta}{\partial y}\right)_e + \left[f + \left(\frac{\partial v}{\partial x}\right)_e - \left(\frac{\partial u}{\partial y}\right)_e \right]\frac{\partial \theta}{\partial e} \right\}. \end{aligned} \tag{6}$$

Letting

$$\begin{aligned} A &= -\frac{\partial v}{\partial e}\left(\frac{\partial \theta}{\partial x}\right)_e \\ B &= \frac{\partial u}{\partial e}\left(\frac{\partial \theta}{\partial y}\right)_e \\ C &= \left[f + \left(\frac{\partial v}{\partial x}\right)_e - \left(\frac{\partial u}{\partial y}\right)_e \right]\frac{\partial \theta}{\partial e} \end{aligned},$$

we then have $P_e = \alpha_e(A + B + C)$.

Performing vertical coordinate transformation and substituting the conversion relationship (4) into expressions for A, B, and C lead to

$$A = -\frac{\partial v}{\partial e}\left(\frac{\partial \theta}{\partial x}\right)_e = -\frac{\partial v}{\partial z}\frac{\partial z}{\partial e}\left[\left(\frac{\partial \theta}{\partial x}\right)_z + \frac{\partial \theta}{\partial z}\left(\frac{\partial z}{\partial x}\right)_e\right]$$

$$B = \frac{\partial u}{\partial e}\left(\frac{\partial \theta}{\partial y}\right)_e = \frac{\partial u}{\partial z}\frac{\partial z}{\partial e}\left[\left(\frac{\partial \theta}{\partial y}\right)_z + \frac{\partial \theta}{\partial z}\left(\frac{\partial z}{\partial y}\right)_e\right]$$

$$C = \left[f + \left(\frac{\partial v}{\partial x}\right)_e - \left(\frac{\partial u}{\partial y}\right)_e\right]\frac{\partial \theta}{\partial e}$$

$$= \left\{f + \left[\left(\frac{\partial v}{\partial x}\right)_z + \frac{\partial v}{\partial z}\left(\frac{\partial z}{\partial x}\right)_e\right] - \left[\left(\frac{\partial u}{\partial y}\right)_z + \frac{\partial u}{\partial z}\left(\frac{\partial z}{\partial y}\right)_e\right]\right\}\frac{\partial \theta}{\partial z}\frac{\partial z}{\partial e}.$$

The underlined terms correspond to horizontal coordinate transformation items. After adding A, B, and C, the horizontal coordinate transformation items cancel each other out, and we have the relation

$$P_e = \alpha_e \vec{\xi}_{ae}\cdot\nabla_e\theta = \alpha_z \vec{\xi}_{az}\cdot\nabla_z\theta = P. \qquad (7)$$

Equation (7) indicates that for a generalized monotonic e coordinate system, when Equation (6) holds for P_e, the final result is strictly equal to P. In other words, PV is independent of the vertical coordinate. From Equations (5) and (6), we obtain PV in a generalized vertical coordinate system.

The coordinate transformation is carried out for the right-hand side of the PV budget (2). The right-hand side of Equation (2) is transformed strictly using the conversion relationships (4) and (5):

where it is seen that the right-hand side of the PV budget equation is also independent of the vertical coordinate.

Substituting Equations (7)–(9) into Equation (2) gives the vertical coordinate independence of the PV budget equation:

$$\frac{dP_e}{dt} = \alpha_e \vec{\xi}_{ae}\cdot\nabla_e\dot{\theta} + \alpha_e\nabla_e\times\vec{F}_f\cdot\nabla_e\theta. \qquad (10)$$

Furthermore, in a monotonic e coordinate system, pressure is expressed by $p = p(x, y, e, t)$. We then have

$$\frac{dp}{dt} = \omega = \frac{\partial p}{\partial t} + u\left(\frac{\partial p}{\partial x}\right)_e + v\left(\frac{\partial p}{\partial y}\right)_e + \dot{e}\frac{\partial p}{\partial e} \qquad (11)$$

and thus

$$\dot{e} = \left[\omega - \frac{\partial p}{\partial t} - u\left(\frac{\partial p}{\partial x}\right)_e - v\left(\frac{\partial p}{\partial y}\right)_e\right]\bigg/\frac{\partial p}{\partial e}. \qquad (12)$$

Therefore, Equation (10) can also be written in Eulerian form in a generalized coordinate system as

$$\frac{\partial P_e}{\partial t} = -\vec{V}\cdot\nabla_e P_e + \alpha_e\vec{\xi}_{ae}\cdot\nabla_e\dot{\theta} + \alpha_e\nabla_e\times\vec{F}_f\cdot\nabla_e\theta, \qquad (13)$$

where $\vec{V} = \left(u, v, \dot{e}\right)$ and $\nabla_e \equiv \left(\frac{\partial}{\partial x}, \frac{\partial}{\partial y}, \frac{\partial}{\partial e}\right)$.

3.3 | PV and PV equation at the surface layer

The hybrid σ–p system is adopted as vertical coordinate in most current climate models. A surface satisfying the partial difference thus needs to be constructed. Let the

$$\alpha_z\vec{\xi}_{az}\cdot\nabla_z\dot{\theta} = \alpha_z\left\{-\frac{\partial v}{\partial z}\left(\frac{\partial \dot{\theta}}{\partial x}\right)_z + \frac{\partial u}{\partial z}\left(\frac{\partial \dot{\theta}}{\partial y}\right)_z + \left[f + \left(\frac{\partial v}{\partial x}\right)_z - \left(\frac{\partial u}{\partial y}\right)_z\right]\frac{\partial \dot{\theta}}{\partial z}\right\}$$
$$= \alpha_e\left\{-\frac{\partial v}{\partial e}\left(\frac{\partial \dot{\theta}}{\partial x}\right)_e + \frac{\partial u}{\partial e}\left(\frac{\partial \dot{\theta}}{\partial y}\right)_e + \left[f + \left(\frac{\partial v}{\partial x}\right)_e - \left(\frac{\partial u}{\partial y}\right)_e\right]\frac{\partial \dot{\theta}}{\partial e}\right\}, \qquad (8)$$
$$= \alpha_e\vec{\xi}_{ae}\cdot\nabla_e\dot{\theta}$$

$$\alpha_z\nabla_z\times\vec{F}_f\cdot\nabla_z\theta = \alpha_z\left\{-\frac{\partial F_y}{\partial z}\left(\frac{\partial \theta}{\partial x}\right)_z + \frac{\partial F_x}{\partial z}\left(\frac{\partial \theta}{\partial y}\right)_z + \left[\left(\frac{\partial F_y}{\partial x}\right)_z - \left(\frac{\partial F_x}{\partial y}\right)_z\right]\frac{\partial \theta}{\partial z}\right\}$$
$$= \alpha_e\left\{-\frac{\partial F_y}{\partial e}\left(\frac{\partial \theta}{\partial x}\right)_e + \frac{\partial F_x}{\partial e}\left(\frac{\partial \theta}{\partial y}\right)_e + \left[\left(\frac{\partial F_y}{\partial x}\right)_e - \left(\frac{\partial F_x}{\partial y}\right)_e\right]\frac{\partial \theta}{\partial e}\right\}, \qquad (9)$$
$$= \alpha_e\nabla_e\times\vec{F}_f\cdot\nabla_e\theta$$

hybrid $\sigma-p$ model levels from top to bottom be $h = 1$, $h = 2$, ..., $h = N$. The model level is an isosurface indicated by h, which describes the surface layer and the space above.

According to the vertical-coordinate independence introduced in Section 3.2, the PV and PV budget equations (Equations (6) and (13)) at the hybrid $\sigma-p$ model level are obtained by setting $e = h$:

$$
\begin{aligned}
P_h &= \alpha_h \vec{\xi}_{ah} \cdot \nabla_h \theta \\
&= \alpha_h \left\{ -\frac{\partial v}{\partial h}\left(\frac{\partial \theta}{\partial x}\right)_h + \frac{\partial u}{\partial h}\left(\frac{\partial \theta}{\partial y}\right)_h \right. \\
&\left. + \left[f + \left(\frac{\partial v}{\partial x}\right)_h - \left(\frac{\partial u}{\partial y}\right)_h \right]\frac{\partial \theta}{\partial h} \right\},
\end{aligned}
\tag{14}
$$

$$
\frac{\partial P_h}{\partial t} = -\vec{V}\cdot\nabla_h P_h + \alpha_h\vec{\xi}_{ah}\cdot\nabla_h\dot\theta + \alpha_h\nabla_h\times\overrightarrow{F_f}\cdot\nabla_h\theta,
\tag{15}
$$

where $\alpha_h = \alpha_z\frac{\partial h}{\partial z}$, $\vec{V} = \left(u, v, \dot h\right)$, $\dot h = \left[\omega - \frac{\partial p}{\partial t} - u\left(\frac{\partial p}{\partial x}\right)_h - v\left(\frac{\partial p}{\partial y}\right)_h\right]/\frac{\partial p}{\partial h}$, and $\nabla_h = \left(\frac{\partial}{\partial x}, \frac{\partial}{\partial y}, \frac{\partial}{\partial h}\right)$.

We substitute $\frac{\partial p}{\partial z} = -\rho g$ and $\alpha_h = \alpha_z\frac{\partial h}{\partial z}$ into Equations (14) and (15) and obtain

$$
P_h = \underbrace{g\left[\frac{\partial v}{\partial p}\left(\frac{\partial \theta}{\partial x}\right)_h - \frac{\partial u}{\partial p}\left(\frac{\partial \theta}{\partial y}\right)_h\right]}_{PV\_horizontal} \underbrace{- g\left[f + \left(\frac{\partial v}{\partial x}\right)_h - \left(\frac{\partial u}{\partial y}\right)_h\right]\frac{\partial \theta}{\partial p}}_{PV\_vertical},
\tag{16}
$$

vertical difference variable. The terms on the right-hand side of Equation (16) are referred to as the PV horizontal and vertical components. The terms in Equation (17) are the local term, advection term, heating term, and friction term. Equations (16) and (17) form a set of equations for PV and the PV budget in the hybrid $\sigma-p$ coordinate system. The surface PV and surface PV budget are obtained from Equations (16)–(18) at the two bottom model levels.

4 | CLIMATE FEATURES OF SURFACE PV

The horizontal component of PV is usually small over the area of a plain, and only the vertical component of PV is used to represent PV. Figure 2 shows the climate mean surface PV and its horizontal and vertical components over the TP in winter and summer. In general, the surface PV increases with latitude, which is mainly due to the *f*-effect. In winter, the maximum surface PV centre is located north of the TP platform (Figure 2a) and the surface PV on the TP is approximately twice that on the eastern plain. In comparison, in summer, the surface PV decreases and its maximum centre shifts to the western TP (Figure 2b). There is a relatively large centre on the north-central TP platform, which is larger than that in western and southern areas. The distribution of the vertical component of the surface PV (Figure 2c,d) is similar to that of the total surface PV in both winter and summer

$$
\begin{aligned}
\frac{\partial P_h}{\partial t} &= \underbrace{-\vec{V}\cdot\nabla_h P_h}_{local} + \underbrace{\alpha_h\vec{\xi}_{ah}\cdot\nabla_h\dot\theta}_{advection} + \underbrace{\alpha_h\nabla_h\times\vec{F}\cdot\nabla_h\theta}_{heating \quad friction} \\
&= -u\frac{\partial P_h}{\partial x} - v\frac{\partial P_h}{\partial y} - \omega_h\frac{\partial P_h}{\partial p} \\
&- g\left\{-\frac{\partial v}{\partial p}\left(\frac{\partial\dot\theta}{\partial x}\right)_h + \frac{\partial u}{\partial p}\left(\frac{\partial\dot\theta}{\partial y}\right)_h + \left[f + \left(\frac{\partial v}{\partial x}\right)_h - \left(\frac{\partial u}{\partial y}\right)_h\right]\frac{\partial\dot\theta}{\partial p}\right\} \\
&- g\left\{-\frac{\partial F_y}{\partial p}\left(\frac{\partial\theta}{\partial x}\right)_h + \frac{\partial F_x}{\partial p}\left(\frac{\partial\theta}{\partial y}\right)_h + \left[f + \left(\frac{\partial F_y}{\partial x}\right)_h - \left(\frac{\partial F_x}{\partial y}\right)_h\right]\frac{\partial\theta}{\partial p}\right\}
\end{aligned},
\tag{17}
$$

where

$$
\omega_h = \left[\omega - \frac{\partial p}{\partial t} - u\left(\frac{\partial p}{\partial x}\right)_h - v\left(\frac{\partial p}{\partial y}\right)_h\right].
\tag{18}
$$

Here the horizontal difference is carried out at the hybrid $\sigma-p$ model level, and the pressure is taken as the

(Figure 2a,b), indicating that the vertical component dominates the surface PV over the main TP platform.

Although the horizontal component of the surface PV is relatively small, it cannot be ignored, especially along the sloping edge of the TP (Figure 2e,f). Figure 2e shows the horizontal component of the surface PV in winter. The component is negative for almost all the TP,
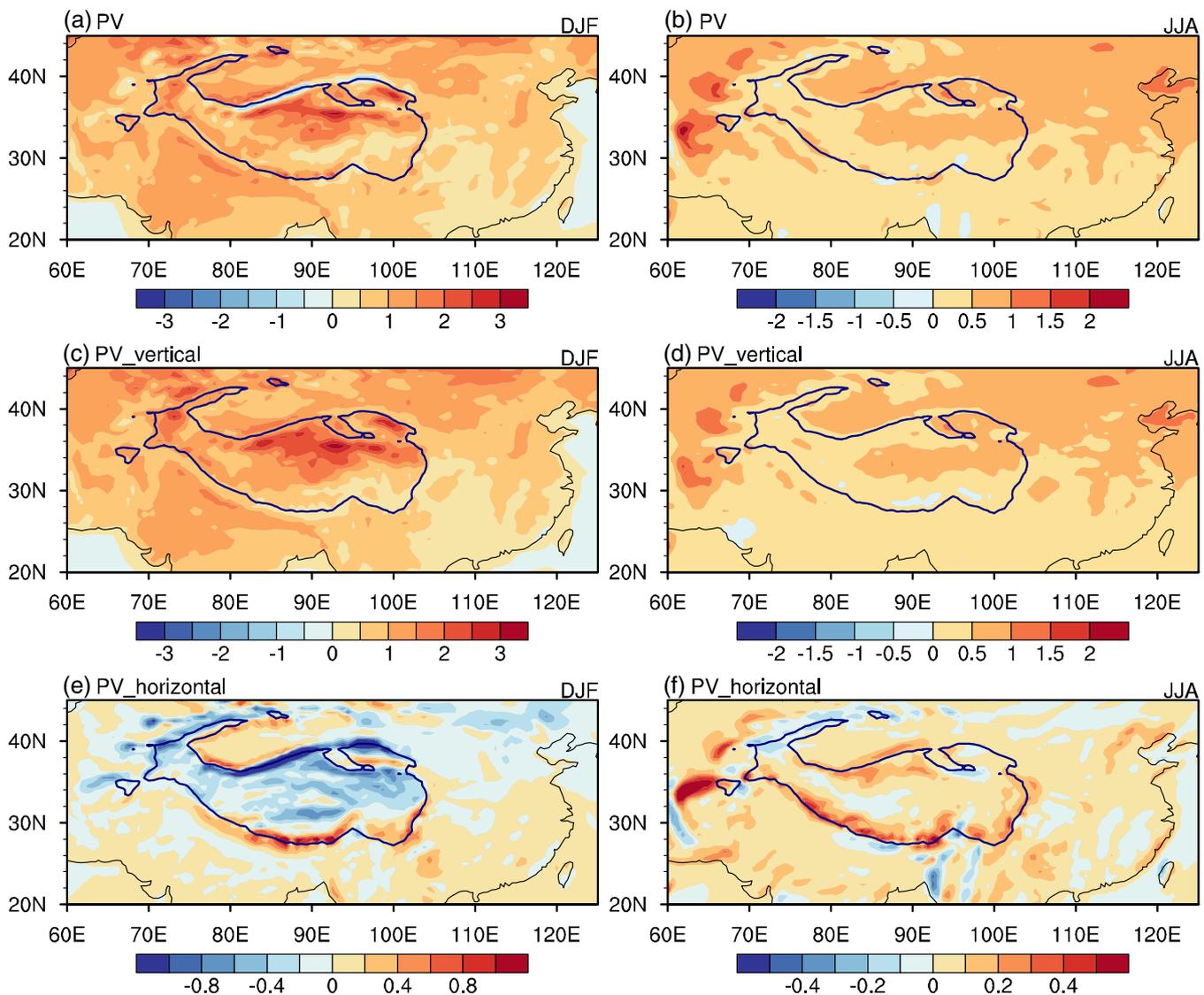
FIGURE 2 Climate mean surface distribution in winter calculated from MERRA2 results for (a) the total PV, (c) the vertical PV component, and (e) the horizontal PV component (units: PVU, 1 PVU = 10^{-6} K m^2 kg^{-1} s^{-1}). (b), (d), (f) are the same as (a), (c), (e), respectively, but for summer. The blue line denotes the TP topographic boundary of 3,000 m

especially along the Kunlun and Tianshan mountains. Positive values are found for the Tarim Basin, the Himalayas, and the southeastern slope of the TP, with the maximum centre located on the southern slope of the TP. Figure 2f shows the horizontal component of the surface PV in summer. The horizontal component is characterized as being greater along the edge of the TP than on the central TP platform. Its maximum centres are located on the eastern Iranian plateau, the Himalayas, the Kunlun Mountains, and the eastern slope of the TP. One of the most striking features is that the absolute value of the horizontal component of the surface PV along the edge of the TP, especially the northern and southern slopes, is larger than that over the flat areas.

The corresponding results of FAMIL2 are shown in Figure 3. The magnitudes of the surface PV and its horizontal and vertical components in the model are larger than those in the reanalysis (Figure 2). This difference in magnitude is mainly due to the difference in the vertical resolution of the surface layer between MERRA2 and FAMIL2. The lowest level in MERRA2 is approximately 60 m above the surface of the TP while that in FAMIL2 is approximately 30 m above the surface. The thickness of the surface layer for the calculation of surface PV is approximately 110 m in MERRA2 and 60 m in FAMIL2. This difference in thickness is amplified in mountain areas because Δp in Equations (16) and (17) is proportional to the surface pressure. Consequently, the
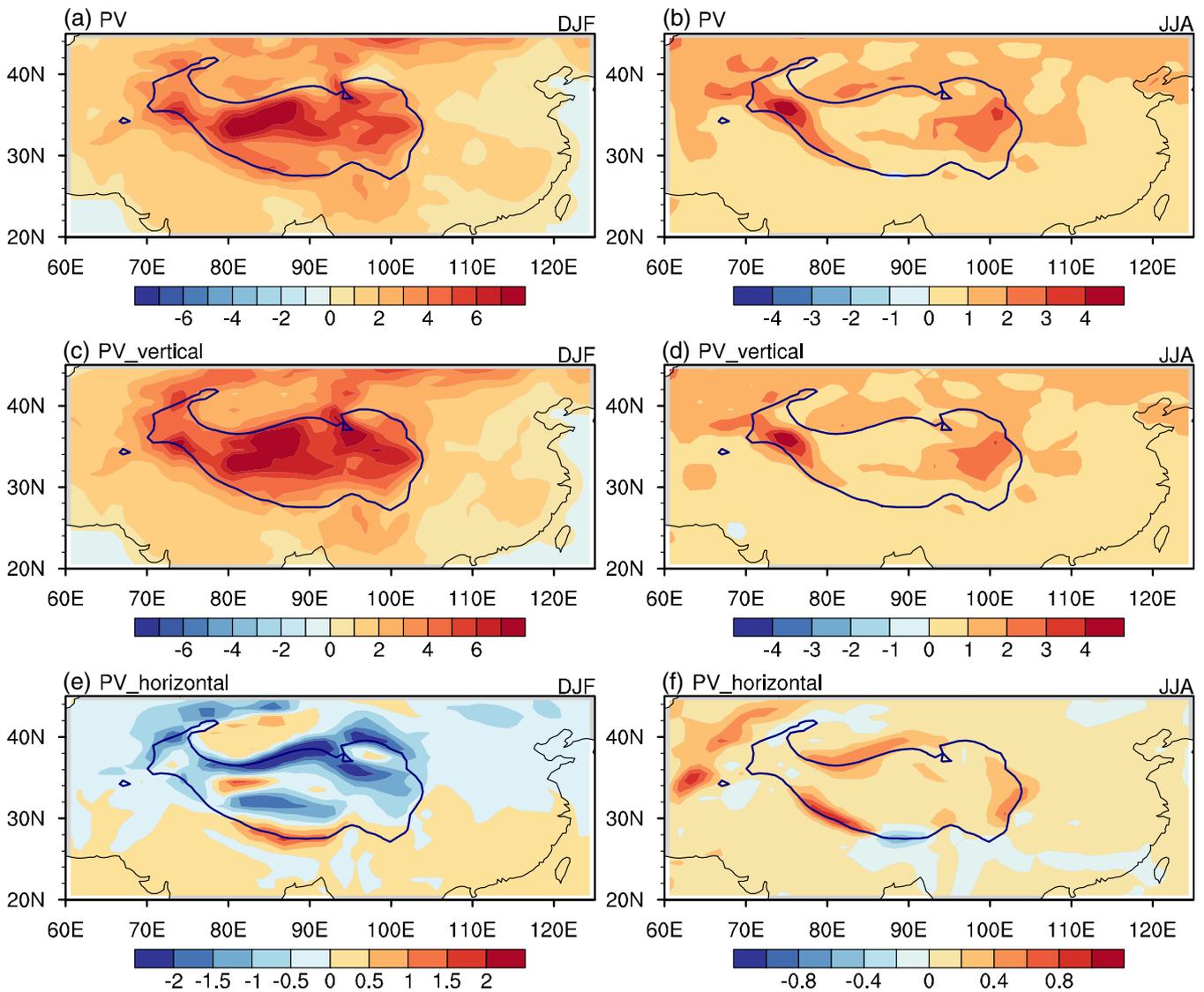
FIGURE 3 Same as Figure 2 but for the results from FAMIL2

magnitude calculated from the FAMIL2 output over the TP (Figure 3) is approximately double that calculated from the MERRA2 data (Figure 2). Despite this, the distributions are similar. In winter, the maximum surface PV centre is located north of the TP platform (Figure 3a) owing to the vertical component of PV (Figure 3c). The positive horizontal component (Figure 3e) is mainly located on the southern slope of the TP and Tarim Basin, and the negative horizontal component covers the TP almost entirely and especially covers the Kunlun and Tianshan mountains near the northern TP. In summer, there is a large positive surface PV centre over the western and eastern TP (Figure 3b). The horizontal component is characterized by the absolute value near the edge of the TP being larger than that on the central TP platform (Figure 3f). Both the MERRA2 and FAMIL2 results show that the absolute value of the horizontal

component of surface PV over the northern and southern slopes of the TP is larger than that over the flat areas.

For further investigation of the importance of the horizontal component of surface PV over the steep northern and southern TP slopes, Figure 4 shows the ratio of the 85°–95°E mean absolute horizontal component of surface PV to the absolute vertical component. According to MERRA2, there are two peaks near the southern and northern slopes of the TP, where the peak value over the southern slope is much higher than that over the northern slope (Figure 4a). Both in winter and summer (Figure 4a), the horizontal component is twice the vertical component near the southern slope and approximately 0.5 times the vertical component near the northern slope of the TP. The ratio calculated from FAMIL2 (Figure 4b) is close to that calculated from

MERRA2 (Figure 4a) but the magnitudes are smaller for FAMIL2 data, which may be attributed to the weaker terrain gradient and coarser horizontal resolution in FAMIL2. Both the results of the reanalysis and model simulation show that on the steep slopes and especially on the southern TP slope, the horizontal component of the surface PV is comparable to or even far in excess of the vertical component.

The horizontal component of the surface PV is further divided into two parts (i.e., $h1 = g\frac{\partial v}{\partial p}\left(\frac{\partial \theta}{\partial x}\right)_h$ and $h2 = -g\frac{\partial u}{\partial p}\left(\frac{\partial \theta}{\partial y}\right)_h$) to explore why it is large on steep terrain. We found that the horizontal component of the surface PV is mainly determined by $h2$, which is the product of the vertical shear of the zonal wind (Figure 5a–d) and the meridional gradient of potential temperature (Figure 5e–h) within the surface layer. In winter, there is a uniform positive mode of $-g\frac{\partial u}{\partial p}$ over the whole TP (Figure 5a,e); in summer (Figure 5b,f), $-g\frac{\partial u}{\partial p}$ has a dipole pattern that is positive on the southern TP and negative on the northern TP, with no specific signals along the steep slopes. However, there is a strong meridional gradient of potential temperature on the southern and northern slopes both in winter (Figure 5c,g) and summer (Figure 5d,h), and a weak meridional gradient of potential temperature mainly occurs on the central TP and other flat areas. The results document that the strong meridional gradient of potential temperature contributes to the formation of the strong horizontal component of surface PV over the TP slopes.

In this section, a comparison of the surface PV based on data at model levels from FAMIL2 and MERRA2 illustrates that although the surface PV is dominated by its vertical component over flat areas, its horizontal component is important over the slopes of the TP, especially over the southern TP slope. The prominent horizontal component of the surface PV over the slopes of the TP is mainly due to the strong in-situ meridional gradient of potential temperature. We therefore highlight that the horizontal component of the surface PV should be included in the analysis. In fact, Wu et al. (1995) documented the importance of the PV horizontal component. They showed that when air parcels move along a slantwise isentropic surface, changes in the horizontal component of PV induce vertical vorticity and stimulate precipitation. Moreover, there is feedback between the precipitation and thermal structure of circulation over the southern TP slope (Wu et al., 2016). The thermal forcing of the TP plays a vital role in the Asian summer monsoon (Wu et al., 2007, 2012, 2018). Therefore, to better understand atmospheric phenomena related to the TP, such as the Asian summer monsoon, a more accurate characterization of the vertical and horizontal components of the surface PV (Equation (16)) is required.

5 | APPLICATION OF THE SURFACE PV BUDGET TO TPV STUDY

A TPV is a specific synoptic system over the TP in boreal summer, with a typical spatial scale of 400–800 km horizontally and 2–3 km vertically. TPVs not only have an important effect on precipitation over the main body of the TP but also are closely related to the rainfall over southwestern and eastern China (Ye and Gao, 1979; Luo et al., 1994; Li et al., 2014). As a result, the formation and evolution of TPVs have received increasing attention. In general, TPVs form mainly over the central–western plateau in the period from June to August and much less so in May and September; the occurrence frequency of the vortices peaks in June; most of the TPVs die out in-situ while some develop and move eastward and a few move
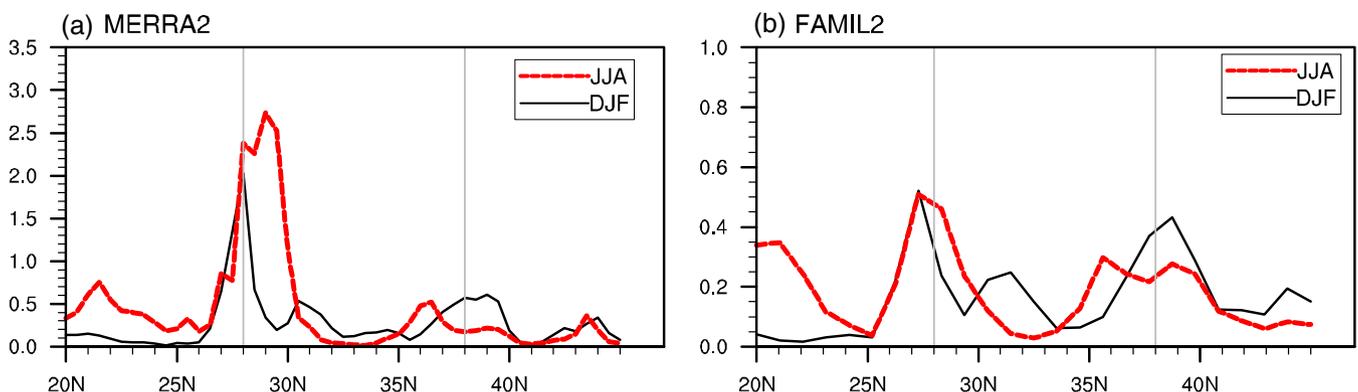

FIGURE 4 Ratio of the 85°–95°E mean absolute horizontal component of the surface PV to the absolute vertical component during winter (DJF) and summer (JJA). (a) MERRA2 result and (b) FAMIL2 result. Grey lines (28°E, 38°E) indicate the edges of the southern and northern TP slopes. ratio=$\frac{85°E-95°E \text{ mean |horizontal component of surface PV|}}{85°E-95°E \text{ mean |vertical component of surface PV|}}$

off the TP (Qiao and Zhang, 1994; Chen *et al.*, 1996; Li *et al.*, 2014).

As an example of applying the surface PV budget equation in practice, we selected a TPV event lasting from 27 to June 29, 2016 as a case study. The synoptic analysis of this process at 500 hPa from the PV perspective was carried out by Ma *et al.* (2019) using MERRA2 data, which provided a weather background for the exploration of the surface PV budget. Instead

of examining the synoptic process and evaluating model bias, we mainly focused on the balance of the PV budget based on Equation (17) and the effect of the heating term.

The occurrence frequency of TPVs peaks in June (Li *et al.*, 2014). Figure 6 shows the climate mean diurnal cycle of the surface PV budget from Lhasa time (LT) 00:00 to LT 21:00 in June. The time interval is 3 hr. In the climate mean state, the contributions of the
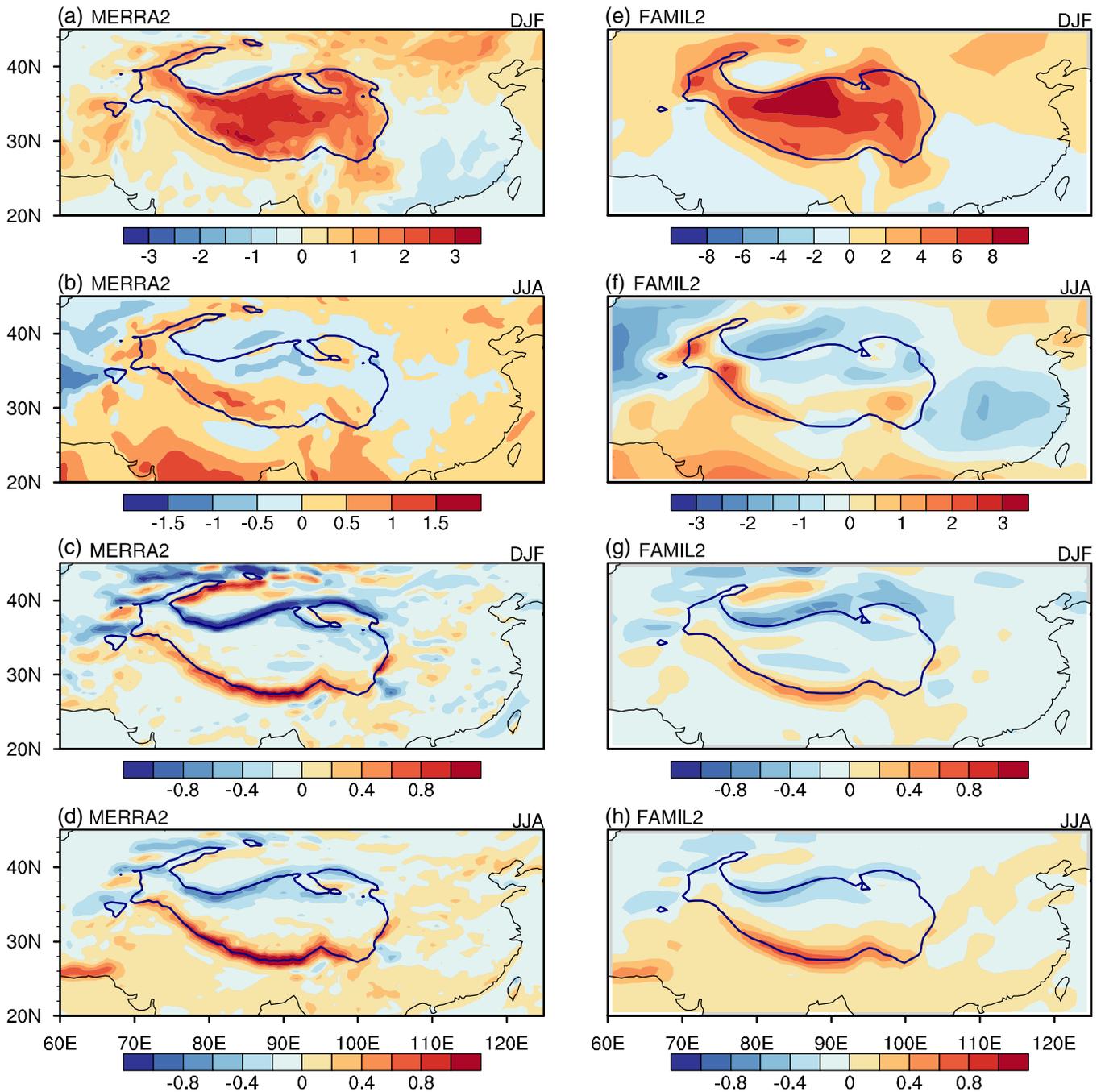

FIGURE 5 Climate mean vertical shear of the zonal wind (first two rows, units: 10^{-2} s^{-1} m^3 kg^{-1}) and meridional potential temperature gradient (last two rows, units: 10^{-4} K m^{-1}) calculated from MERRA2 (a–d) and FAMIL2 (e–h) at the surface in boreal winter and summer. The blue line denotes the TP topographic boundary of 3,000 m
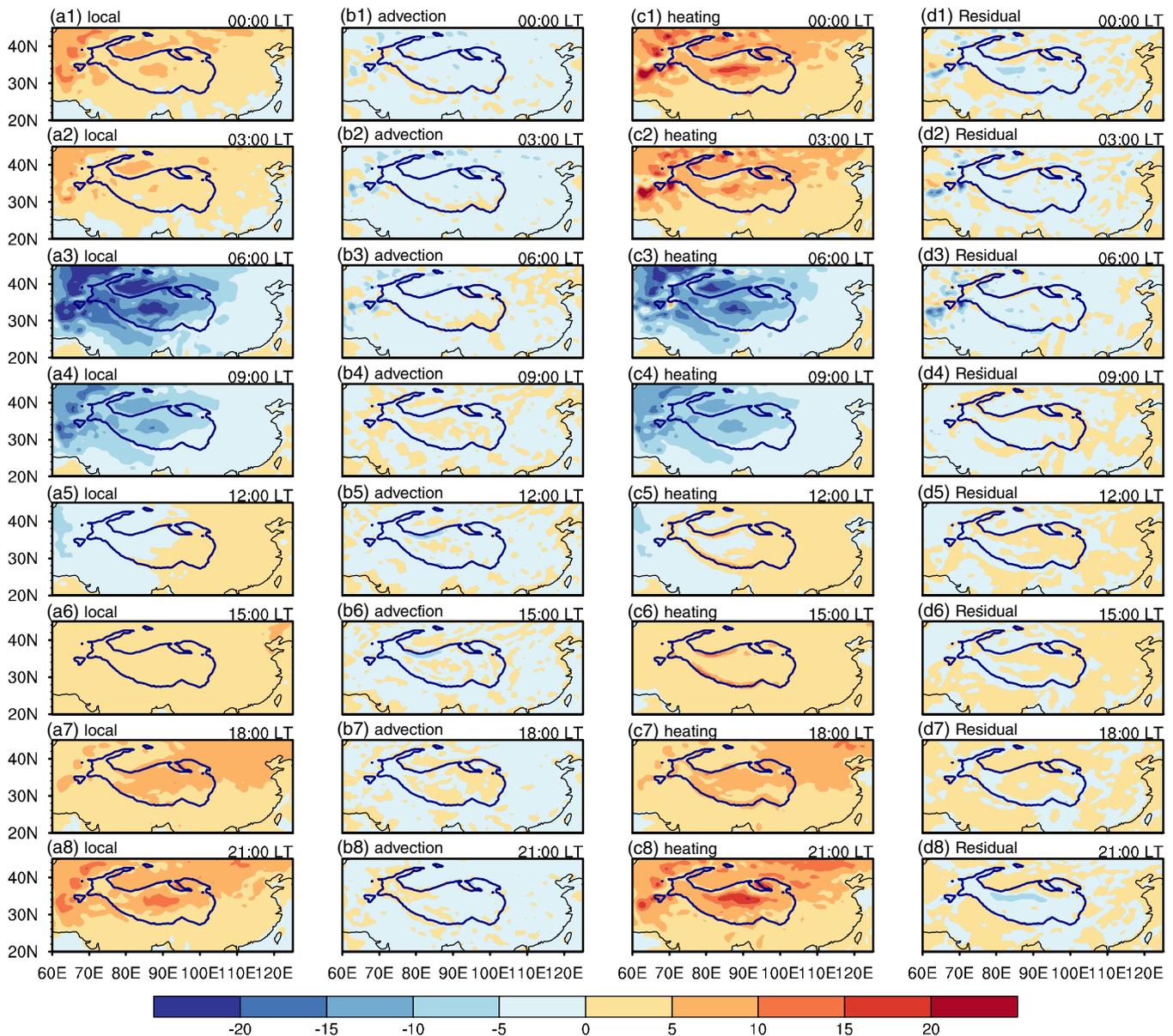
FIGURE 6 Climate mean (2010–2017) diurnal cycle from LT 00:00 (top row) to LT 21:00 (bottom row) in 3-hour intervals of each term (units: 10^{-5} PVU s^{-1}) in surface PV budget Equation (17) for June: (a1)–(a8) local term, (b1)–(b8) advection term, (c1)–(c8) heating term, and (d1)–(d8) residual term. The blue line denotes the TP topographic boundary of 3,000 m

advection term (Figure 6b1–b8) and residual term (Figure 6d1–d8) are small and can be neglected. The local term (Figure 6a1–a8) is mainly balanced by the heating term (Figure 6c1–c8). The local change of surface PV (Figure 6a1–a8) and diabatic heating (Figure 6c1–c8) show a prominent diurnal cycle with a positive value from afternoon to midnight (LT 15:00–03:00) and negative value from early morning to noon (LT 06:00–12:00). The minimum appears at LT 06:00 over the central-western TP while the maximum appears from LT 21:00 to LT 03:00, implying that the surface PV generated mainly from afternoon to midnight is consumed in the

morning. Li *et al.* (2014) documented that the occurrence frequency of the TPVs processes a robust diurnal variation with a maximum from evening to midnight and a minimum from early morning to noon. Comparing the results of Li *et al.* (2014) (see their Figure 2) with the results of the present study (Figure 6), we infer that the TPVs preferably form at night when the surface PV is generated quickly owing to the strong effect of surface diabatic heating. Additionally, the prominent diurnal cycle of the surface PV budget over the TP is stronger than that in the plain area, indicating the TP is an important area of surface PV variation.

The TPV case considered in this study occurred late at night on June 27, 2016, corresponding to a period of strong PV generation associated with surface diabatic heating in the climate mean state. The TPV developed and moved on the TP on 28 and 29 June and moved off the TP on 30 June (Ma et al., 2019). To examine the balance of the surface PV budget equation during the TPV evolution, the time series of each term in Equation (17) averaged over the rectangle (20°–45°N, 60°–125°E) was calculated according to MERRA2 and FAMIL2 output at the surface. The time covered the formation and evolution of the TPV from LT 6:00 on 27 June to LT 3:00 on June 30, 2016. Results are shown in Figure 7. The coefficient of correlation between the local term on the left side of Equation (17) and the sum2 (advection plus heating) term on the right side of Equation (17) exceeds 0.95 for both MERRA2 (Figure 7a) and FAMIL2 (Figure 7b), surpassing the 99% significance level. Consequently, the residual (local minus sum2) term (Figure 7a,b) is very small. In MERRA2 (Figure 7a) and FAMIL2 (Figure 7b), the advection term is smaller than the heating term, which means the heating term dominates the sum2 term and local term. Although the magnitudes in FAMIL2 (Figure 7b) are larger than their counterparts in MERRA2 (Figure 7a), as previously mentioned, the diurnal cycle of each term is similar in these two datasets, with the minimum around sunrise and the maximum around sunset, indicating an increase in PV from afternoon to midnight but a decrease from early morning to noon. The small residual and the consistency in the PV budget between MERRA2 and FAMIL2 indicate that the surface PV budget Equation (17) is well balanced in the synoptic process.

The coefficients of correlation between the local term and heating term and between the local term and advection term during the TPV process are given in Table 1. The correlation between the local term and heating term is as high as 0.986 and 0.966 for MERRA2 and FAMIL2, surpassing the 99% significance level in both datasets. However, the correlation between the local term and advection term is weak and does not surpass the

TABLE 1 Coefficient of correlation between the local term and the sum2 (heating plus advection) term (second row), heating term (third row), and advection term (bottom row) for MERRA2 (middle column) and FAMIL2 (rightmost column) during the TPV process from 27 to June 29, 2016

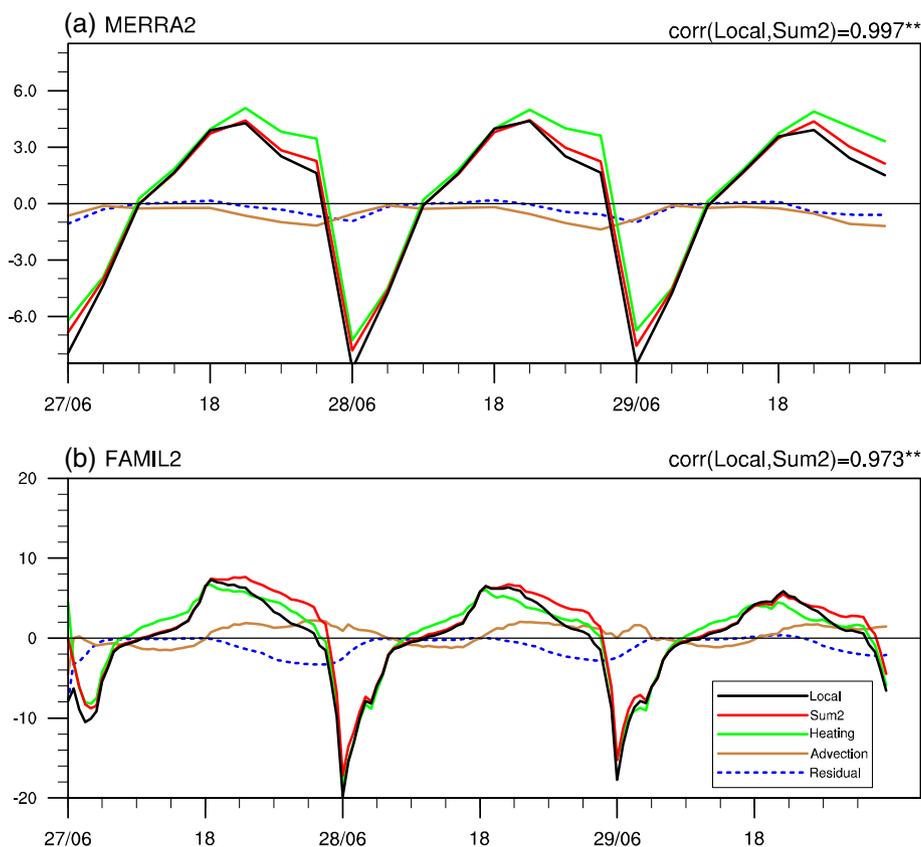| Correlation (local term)	MERRA2	FAMIL2
Sum2 term	0.997**	0.973**
Heating term	0.986**	0.966**
Advection term	−0.124	0.127

**Surpassing the 99% significance level.

FIGURE 7 Evolution from LT 6:00 on 27 June to LT 3:00 on 30 June 2016 and averaged over the rectangle (20°–45°N, 60°–125°E) of the local term (black curve), sum of the advection and heating terms (red curve, sum2), heating term (green curve), advection term (brown curve), and residual term (blue dashed curve) at the surface based on Equation (17). (a) MERRA2, (b) FAMIL2. Units: 10^{-11} K m^2 kg^{-1} s^{-2}. "**" indicates surpassing the 99% significance level

significance test. The results show that diabatic heating plays an important role in the local change of surface PV.

The lowest hybrid $\sigma-p$ levels in MERRA2 and FAMIL2 have different altitudes. Therefore, for comparison of the evolutions of the PV budget in the two model outputs, each term in Equation (17) calculated from MERRA2 and FAMIL2 is interpolated to the same pressure level (500 hPa). The results from MERRA2 reanalysis for the period from 27 to June 29, 2016 are shown in Figure 8. From the top row to the bottom rows are the local term, sum2 term, advection term, heating term, and residual term at LT 15:00 while the left, middle, and right columns are respectively for 27, 28, and June 29, 2016. The residual term is small except at the northern edge (Figure 8a5–c5), and the patterns of the local term (Figure 8a1–c1) and sum2 term (Figure 8a2–c2) are similar during the TPV generation (left column of Figure 8), development (middle), and movement (right) stages, indicating a reasonable balance of the PV budget

based on Equation (17), as previously discussed. During the development stage of the TPV, there is positive PV generation to the southeast of the TPV centre (Figure 8b1), which leads to the local PV increase and southeastward movement of the growing TPV. Moreover, the positive PV generation (Figure 8b1) is primarily due to the heating term (Figure 8b4), which means that the diabatic heating effect has a noticeable effect on the positive PV generation and the movement of the TPV. However, the advection term (Figure 8b3) makes the opposite contribution and tends to cancel part of the diabatic heating effect (Figure 8b4). During the movement stage, although the negative advection term (Figure 8c3) is stronger than that in the development stage (Figure 8b3), the positive diabatic heating effect (Figure 8c4) is more powerful than the negative advection effect, resulting in strong positive PV generation (Figure 8c1) to the south of the TPV centre. Finally, the TPV further strengthens and moves off the TP.
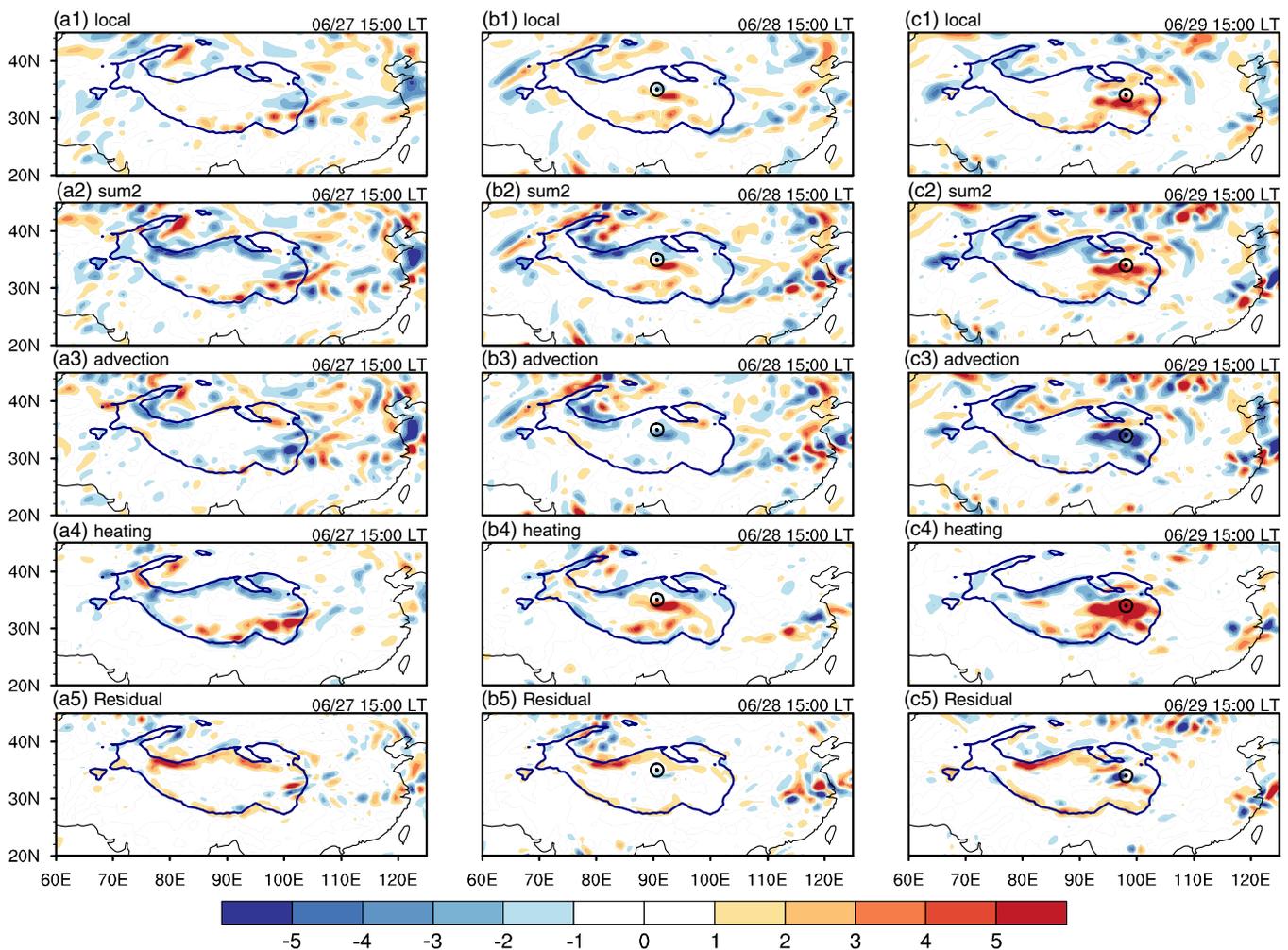

FIGURE 8 Distributions at 500 hPa of (a1–c1) the PV local term, (a2–c2) the sum of the advection and heating (sum2) terms, (a3–c3) the advection term, (a4–c4) the heating term, and (a5–c5) the residual term at local time 15:00 in Lhasa on 27 (a1–a5), 28 (b1–b5), and 29 (c1–c5) June 2016. Units: 10^{-11} K m^2 kg^{-1} s^{-2}. The black dot and circle indicate the TPV
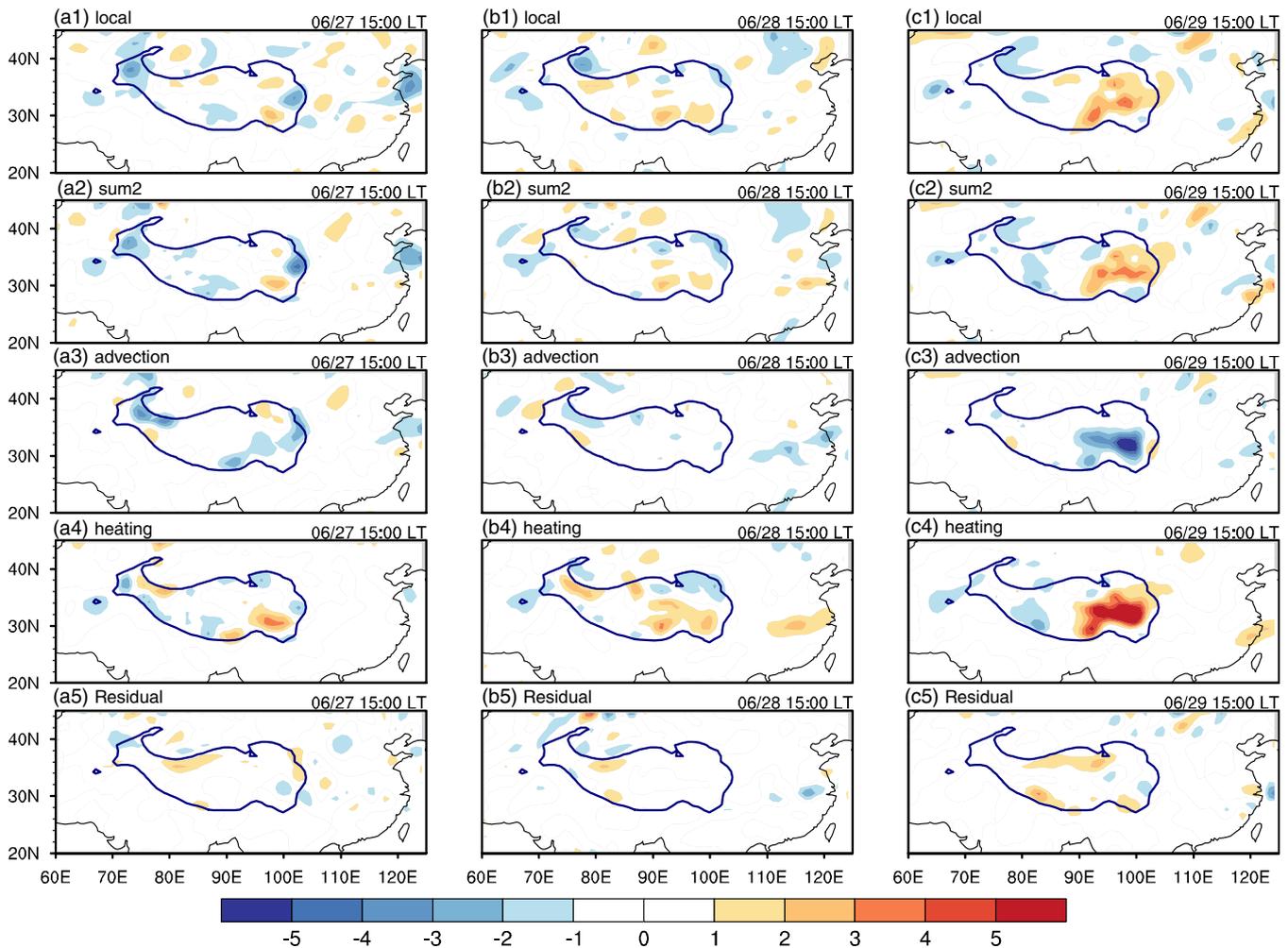
FIGURE 9 Same as Figure 8 but for the results from FAMIL2

The results obtained from FAMIL2 (Figure 9) are smoother than those obtained from MERRA2 (Figure 8), which is mainly due to the coarser horizontal resolution and higher time resolution. Despite this, the distributions are similar. As expected, the residual term (Figure 9a5–c5) is small in FAMIL2, and the patterns of the local term (Figure 9a1–c1) and the sum2 term (Figure 9a2–c2) are similar, implying a good balance of the PV budget Equation (17). The positive PV generation (Figure 9a1–c1) is dominated by the heating term (Figure 9a4–c4), especially in the movement stage (Figure 9c1,c4). The advection term (Figure 9b3–c3) mainly contributes to the in-situ PV reduction and tends to partly cancel the strong diabatic heating effect (Figure 9a4–c4). These results agree with those of MERRA2. The results of FAMIL2 and MERRA2 consistently show that diabatic heating has an important effect on the development and movement of the TPV centre associated with positive PV generation. The results of dynamic analyses here are consistent with the results of previous statistical studies (e.g., Luo *et al.*, 1994; Li *et al.*, 2002; Li *et al.*, 2016), which showed

that the occurrence, development, and extinction of the TPV are closely related to the diabatic heating effect.

The results presented in this section demonstrate that the surface PV budget Equation (17) is well balanced both in the climate mean state and synoptic process. The contribution of diabatic heating with a negative peak in early morning and positive peak from evening to midnight dominates the diurnal cycle of the surface PV budget. The case study further shows that diabatic heating has an essential effect on the development and movement of the TPV centre associated with positive PV generation.

6 | SUMMARY AND DISCUSSION

6.1 | Summary

The studies of Haynes and McIntyre (1987, 1990) and Hoskins (1991) demonstrated that the budget of globally integrated PV in the atmosphere is determined by the generation of PV at the Earth's surface. However, because of

the complexity of terrain, wholly characterizing the features and budget of surface PV is a great challenge. The present study revealed the features of surface PV and provided a stepping stone to investigate the surface PV budget. An algorithm for evaluating the surface PV and its budget was derived, and the features and budget of surface PV based on the MERRA2 model level reanalysis and FAMIL2 model level data were diagnosed. The main conclusions drawn from the results of the study are as follows:

1. Forms of the PV and PV budget equation are independent of coordinates; that is, they are identical for all vertical coordinate systems.
2. The surface PV is dominated by its vertical component over flat areas in both boreal winter and summer. However, the horizontal component of the surface PV is important over the slopes of the TP, being more than twice the vertical component over the steep southern slope of the TP. The prominent horizontal component of the surface PV is mainly attributed to the strong in-situ meridional gradient of the potential temperature. On steep terrain, neglecting the horizontal component of surface PV can lead to large errors in capturing the surface PV structure and associated dynamic processes. The results indicate that the complete expression of PV (Equation (16)) can help reveal the fine-scale structure and dynamic effect of the surface PV.
3. Surface PV budget analyses showed that the surface PV budget Equation (17) is well balanced both in the climate mean state and synoptic process. The surface PV budget and the diabatic heating are characterized by a prominent diurnal cycle; the prominent diurnal cycle signal is stronger over the TP than in plain areas, indicating that the TP is an important area of surface PV variation. The contribution of diabatic heating that has a minimum in the early morning and maximum from evening to midnight dominates the diurnal cycle of the surface PV budget. The case study of the TPV further indicates that diabatic heating has an important effect on the development and movement of the TPV centre associated with positive PV generation.

6.2 | Discussion

To further reveal the important roles of surface PV and its budget in atmospheric general circulation, several issues are highlighted below for future study.

The lowest model levels of MERRA2 and FAMIL2 are at some distance (approximately 60 m and 30 m, respectively) from the Earth's surface. It has been demonstrated that the calculation of the surface PV is sensitive to the vertical resolution of the model near the surface layer. An improved surface layer presentation in the model is conducive to a better evaluation of the surface PV. Moreover, the present study did not explicitly calculate the friction term but instead incorporated the effects of the friction term into the residual term. It is noted that the residual term is the result of the combined effects of transient diffusion and friction, not just the friction term. Hoskins (1991) noted that there is a constraint in linking friction to diabatic heating, and this constraint links "westerlies" and "cooling" as well as "easterlies" and "heating" in an average sense. There are questions concerning the role of friction in the PV budget that need to be addressed in future work.

The diabatic heating is important to the surface PV budget both for the climate mean state and synoptic process. However, how diabatic heating originates, how it contributes to the formation of the TPV, and how it interacts with precipitation, especially on the diurnal timescale, are still unclear and require further study.

White et al. (2018) and Ren et al. (2019) showed the different topographic forcing have different impacts on the atmospheric circulation. Revealing the link between the surface PV in different regions and atmospheric circulation also requires further study.

ORCID
Chen Sheng 🄳 https://orcid.org/0000-0003-0920-3237

REFERENCES
Aebischer, U. and Schär, C. (1996) Low-level potential vorticity and cyclogenesis to the lee of the alps. *Journal of the Atmospheric Sciences*, 55, 186–207. https://doi.org/10.1175/1520-0469(1998)0552.0.CO;2.

Banzon, V., Smith, T.M., Chin, T.M., Liu, C. and Hankins, W. (2016) A long-term record of blended satellite and in situ sea-surface temperature for climate monitoring, modeling and environmental studies. *Earth System Science Data*, 8, 165–176. https://doi.org/10.5194/essd-8-165-2016.

Bao, Q., Wu, X.F., Li, J.X., Wang, L., He, B., Wang, X.C., Liu, Y.M. and Wu, G.X. (2018) Outlook for El Niño and the Indian ocean

dipole in autumn-winter 2018–2019. *Chinese Science Bulletin*, 63, 73–78. https://doi.org/10.1360/N972018-00913.

Cao, J. and Xu, Q. (2011) Computing hydrostatic potential vorticity in terrain-following coordinates. *Monthly Weather Review*, 139, 2955–2961. https://doi.org/10.1175/MWR-D-11-00083.1.

Chen, B.M., Qian, Z.A. and Zhang, L.S. (1996) Numerical simulation of formation and development of vortices over the Qinghai-Xizang Plateau in summer. *Chinese Journal of Atmospheric Sciences*, 20, 491–502.

Egger, J., Hoinka, K.P. and Spengler, T. (2015) Aspects of potential vorticity fluxes: climatology and impermeability. *Journal of the Atmospheric Sciences*, 72, 3257–3267. https://doi.org/10.1175/JAS-D-14-0196.1.

Ertel, H. (1942) Ein neuer hydrodynamische wirbelsatz. *Meteorologische Zeitschrift Braunschweig*, 59, 33–49.

Flamant, C., Richard, E., Schar, C., Rotunno, R., Nance, L., Sprenger, M. and Benoit, R. (2004) The wake south of the alps: dynamics and structure of the lee-side flow and secondary potential vorticity banners. *Quarterly Journal of the Royal Meteorological Society*, 130, 1275–1303. https://doi.org/10.1256/qj.03.17.

Flohn, H. (1957) Large-scale aspects of the "summer monsoon" in South and East Asia. *Journal of the Meteorological Society of Japan*, 35, 180–186.

Haynes, P.H. and McIntyre, M.E. (1987) On the evolution of vorticity and potential vorticity in the presence of diabatic heating and frictional or other forces. *Journal of the Atmospheric Sciences*, 44, 828–841. https://doi.org/10.1175/1520-0469(1987)044<0828:OTEOVA>2.0.CO;2.

Haynes, P.H. and McIntyre, M.E. (1990) On the conservation and impermeability theorems for potential vorticity. *Journal of the Atmospheric Sciences*, 47, 2021–2031. https://doi.org/10.1175/1520-0469(1990)047<2021:OTCAIT>2.0.CO;2.

He, B., Bao, Q., Wang, X.C., Zhou, L.J., Wu, X.F., Liu, Y.M., Wu, G.X., Chen, K.J., He, S.C., Hu, W.T., Li, J.D., Li, J.X., Nian, G.K., Wang, L., Yang, J., Zhang, M.H. and Zhang, X.Q. (2019) CAS FGOALS-f3-L model datasets for CMIP6 historical atmospheric model intercomparison project simulation. *Advances in Atmospheric Sciences*, 36, 771–778. https://doi.org/10.1007/s00376-019-9027-8.

He, B., Liu, Y.M., Wu, G.X., Bao, Q., Zhou, T.J., Wu, X.F., Wang, L., Li, J.D., Wang, X.C., Li, J.X., Zhang, X.Q., Sheng, C. and Tang, Y.Q. (2020) CAS FAMIL2-f3-L model datasets for CMIP6 GMMIP tier-1 and tier-3 experiments. *Advances in Atmospheric Sciences*, 37, 18–28. https://doi.org/10.1007/s00376-019-9085-y.

Held, I.M. and Schneider, T. (1999) The surface branch of the zonally averaged mass transport in the troposphere. *Journal of the Atmospheric Sciences*, 56, 1688–1697. https://doi.org/10.1175/1520-0469(1999)056<1688:TSBOTZ>2.0.CO;2.

Hoke, J.E. and Anthes, R.A. (1976) The initialization of numerical models by a dynamic-initialization technique. *Monthly Weather Review*, 104, 1551–1556. https://doi.org/10.1175/1520-0493(1976)104<1551:TIONMB>2.0.CO;2.

Hoskins, B.J. (1991) Towards a PV-θ view of the general circulation. *Tellus*, 43AB, 27–35.

Hoskins, B.J. (1997) A potential vorticity view of synoptic development. *Meteorological Applications*, 4, 325–334. https://doi.org/10.1017/S1350482797000716.

Hoskins, B.J. (2015) Potential vorticity and the PV perspective. *Advances in Atmospheric Sciences*, 32, 2–9. https://doi.org/10.1007/s00376014-0007-8.

Hoskins, B.J., McIntyre, M.E. and Robertson, A.W. (1985) On the use and significance of isentropic potential vorticity maps. *Quarterly Journal of the Royal Meteorological Society*, 111, 877–946. https://doi.org/10.1002/qj.49711147002.

Li, G.P., Lu, H.G., Huang, C.H., Fan, Y.Y. and Zhang, B. (2016) A climatology of the surface heat source on the Tibetan Plateau in summer and its impacts on the formation of the Tibetan Plateau vortex. *Chinese Journal of Atmospheric Sciences*, 40, 131–141. https://doi.org/10.3878/j.issn.1006-9895.1504.15125.

Li, G.P., Zhao, B.J. and Yang, J.Q. (2002) A dynamical study of the role of surface sensible heating in the structure and intensification of the Tibetan Plateau vortices. *Chinese Journal of Atmospheric Sciences*, 26, 519–525. https://doi.org/10.3878/j.issn.1006-9895.2002.04.09.

Li, J.X., Bao, Q., Liu, Y.M., Wu, G.X., Wang, L., He, B., Wang, X.C. and Li, J.D. (2019) Evaluation of FAMIL2 in simulating the climatology and seasonal-to-interannual variability of tropical cyclone characteristics. *Journal of Advances in Modeling Earth Systems*, 11, 1117–1136. https://doi.org/10.1029/2018MS001506.

Li, L., Zhang, R.H. and Wen, M. (2014) Diurnal variation in the occurrence frequency of the Tibetan Plateau vortices. *Meteorology and Atmosphere Physics*, 125, 135–144. https://doi.org/10.1007/s00703-014-0325-5.

Li, Z., Fei, J.F., Huang, X.G. and Cheng, X.P. (2017) A computational method of Ertel potential vorticity in terrain-following coordinates. *Acta Meteorologica Sinica*, 75, 1011–1026. https://doi.org/10.11676/qxxb2017.064.

Lin, S.J. (2004) A "vertically lagrangian" finite-volume dynamical core for global models. *Monthly Weather Review*, 132, 2293–2307. https://doi.org/10.1175/1520-0493(2004)1322.0.CO;2.

Liu, Y.M., Hoskins, B.J. and Blackburn, M. (2007) Impact of Tibetan orography and heating on the summer flow over Asia. *Journal of the Meteorological Society of Japan*, 85B, 1–19. https://doi.org/10.2151/jmsj.85B.1.

Lucchesi, R. (2012) File Specification for MERRA Products. GMAO Office Note No. 1 (Version 2.3), 87 pp. Available at: https://gmao.gsfc.nasa.gov/pubs/docs/Lucchesi528.pdf [Accessed 18th April 2019].

Luo, D.H., Chen, X.D., Dai, A.G. and Simmonds, L. (2018a) Changes in atmospheric blocking circulations linked with winter arctic warming: a new perspective. *Journal of Climate*, 31, 7661–7678. https://doi.org/10.1175/JCLI-D-18-0040.1.

Luo, D.H., Chen, X.D. and Feldstein, S.B. (2018b) Linear and nonlinear dynamics of North Atlantic oscillations: a new thinking of symmetry breaking. *Journal of the Atmospheric Sciences*, 75, 1955–1977. https://doi.org/10.1175/JAS-D-17-0274.1.

Luo, S.W., He, M.L. and Liu, X.D. (1994) Study on the vortex of the Qinghai-Xizang (Tibet) Plateau in summer. *Science in China (Series B)*, 37, 601–612. https://doi.org/10.1007/BF00717371.

Ma, T., Liu, Y.M., Wu, G.X., Mao, J.Y. and Zhang, G.S. (2019) Potential vorticity diagnosis on the formation, development and eastward movement of a Tibetan Plateau vortex and it's influence on the downstream precipitation. *Chinese Journal of the Atmospheric Sciences*. https://doi.org/10.3878/j.issn.1006-9895.1904.18275.

Ma, T.T., Wu, G.X., Liu, Y.M., Jiang, Z.H. and Yu, J.H. (2019) Impact of surface potential vorticity density forcing over the Tibetan Plateau on the South China extreme precipitation in

January 2008. Part I: Data analysis. *Journal of Meteorological Research*, 33, 400–415. https://doi.org/10.1007/s13351-019-8604-1.

Ortega, S., Webster, P.J., Toma, V. and Chang, H.R. (2018) The effect of potential vorticity fluxes on the circulation of the tropical upper troposphere. *Quarterly Journal of the Royal Meteorological Society*, 144, 848–860. https://doi.org/10.1002/qj.3261.

Putman, W.M. and Lin, S.J. (2007) Finite-volume transport on various cubed-sphere grids. *Journal of Computational Physics*, 227, 55–78. https://doi.org/10.1016/j.jcp.2007.07.022.

Qiao, Q.M. and Zhang, Y.G. (1994) *Synoptic Meteorology of the Tibetan Plateau and its Effect on the Near Areas*. Beijing, China: China Meteorological Press 251 pp.

Ren, R.C., Wu, G.X., Cai, M., Sun, S.Y., Liu, X. and Li, W.P. (2014) Progress in research of stratosphere-troposphere interactions: application of isentropic potential vorticity dynamics and the effects of the Tibetan Plateau. *Journal of Meteorological Research*, 28, 714–731. https://doi.org/10.1007/s13351-014-4026-2.

Ren, R.C., Xia, X. and Rao, J. (2019) Topographic forcing from East Asia and North America in the northern winter stratosphere and their mutual interference. *Journal of Climate*, 32, 8639–8658. https://doi.org/10.1175/JCLI-D-19-0107.1.

Reynolds, R.W., Smith, T.M., Liu, C., Chelton, D.B., Casey, K.S. and Schlax, M.G. (2007) Daily high-resolution-blended analyses for sea surface temperature. *Journal of Climate*, 20, 5473–5496. https://doi.org/10.1175/2007jcli1824.1.

Rienecker, M.M., Suarez, M.J., Gelaro, R., Todling, R., Bacmeister, J., Liu, E., Bosilovich, M.G., Schubert, S.D., Takacs, L., Kim, G.K., Bloom, S., Chen, J., Collins, D., Conaty, A., da Silva, A., Gu, W., Joiner, J., Koster, R.D., Lucchesi, R., Molod, A., Owens, T., Pawson, S., Pegion, P., Redder, C.R., Reichle, R., Robertson, F.R., Ruddick, A.G., Sienkiewicz, M. and Woollen, J. (2011) MERRA: NASA's modern-Era retrospective analysis for research and applications. *Journal of Climate*, 24, 3624–3648. https://doi.org/10.1175/JCLI-D-11-00015.1.

Rossby, C.G. (1940) Planetary flow patterns in the atmosphere. *Quarterly Journal of the Royal Meteorological Society*, 66, 68–87.

Schar, C., Sprenger, M., Luthi, D., Jiang, Q.F., Smith, R.B. and Benoit, R. (2003) Structure and dynamics of an alpine potential-vorticity banner. *Quarterly Journal of the Royal Meteorological Society*, 129, 825–855. https://doi.org/10.1256/qj.02.47.

Schneider, T. (2005) Zonal momentum balance, potential vorticity dynamics, and mass fluxes on near-surface isentropes. *Journal of the Atmospheric Sciences*, 62, 1884–1900. https://doi.org/10.1175/JAS3341.1.

White, R.H., Battisti, D.S. and Sheshadri, A. (2018) Orography and the boreal winter stratosphere: the importance of the Mongolian mountains. *Geophysical Research Letters*, 45, 2088–2096. https://doi.org/10.1002/2018GL077098.

Wu, G.X., Cai, Y.P. and Tang, X.J. (1995) Moist potential vorticity and slantwise vorticity development. *Acta Meteorologica Sinica*, 53, 387–405. https://doi.org/10.11676/qxxb1995.045.

Wu, G.X., Liu, Y.M., He, B., Bao, Q. and Wang, Z.Q. (2018) Review of the impact of the Tibetan Plateau sensible heat driven air-pump on the Asian summer monsoon. *Chinese Journal of the Atmospheric Sciences*, 42, 488–504. https://doi.org/10.3878/j.issn.1006-9895.1801.17279.

Wu, G.X., Liu, Y.M., He, B., Duan, A.M. and Jin, F.F. (2012) Thermal controls on the Asian summer monsoon. *Scientific Reports*, 2, 404. https://doi.org/10.1038/srep00404.

Wu, G.X., Liu, Y.M., Wang, T.M., Wan, R.J., Liu, X., Li, W.P., Wang, Z.Z., Zhang, Q., Duan, A.M. and Liang, X.Y. (2007) The influence of mechanical and thermal forcing by the Tibetan Plateau on Asian climate. *Journal of Hydrometeorology*, 8, 770–789. https://doi.org/10.1175/jhm609.1.

Wu, G.X., Zhuo, H.F., Wang, Z.Q. and Liu, Y.M. (2016) Two types of summertime heating over the Asian large-scale orography and excitation of potential-vorticity forcing I. Over Tibetan Plateau. *Science China Earth Sciences*, 59, 1209–1222. https://doi.org/10.1360/N072015-00519.

Xu, X.D., Zhao, T.L., Shi, X.H. and Lu, C.G. (2015) A study of the role of the Tibetan Plateau's thermal forcing in modulating rainband and moisture transport in eastern China. *Acta Meteorologica Sinica*, 73, 20–35. https://doi.org/10.11676/qxxb2014.051.

Yanai, M.H., Li, C.F. and Song, Z.S. (1992) Seasonal heating of the Tibetan Plateau and its effects on the evolution of the Asian summer monsoon. *Journal of the Meteorological Society of Japan*, 70, 319–351. https://doi.org/10.2151/jmsj1965.70.1B_319.

Ye, D.Z. and Gao, Y.X. (1979) *The Meteorology of the Qinghai–Xizang (Tibet) Plateau*. Beijing, China: Science Press 278 pp.

Ye, D.Z., Luo, S.W. and Zhu, B.Z. (1957) The wind structure and heat balance in the lower troposphere over Tibetan Plateau and its surroundings. *Acta Meteorologica Sinica*, 28, 108–121. https://doi.org/10.11676/qxxb1957.010.

Yu, J.H., Liu, Y.M., Ma, T.T. and Wu, G.X. (2019) Impact of surface potential vorticity density forcing over the Tibetan Plateau on the South China extreme precipitation in January 2008. Part II: Numerical simulation. *Acta Meteorologica Sinica*, 33, 416–432. https://doi.org/10.1007/s13351-019-8606-z.

Zhao, L. and Ding, Y.H. (2009) Potential vorticity analysis of cold air activities during the East Asian summer monsoon. *Chinese Journal of the Atmospheric Sciences*, 33, 359–374. https://doi.org/10.3878/j.issn.1006-9895.2009.02.14.